Yu, C., Vavryčuk, V., Adamová, P., Bohnhoff, M. (2018): Moment tensors of induced microearthquakes in The Geysers geothermal reservoir from broadband seismic recordings: Implications for faulting regime, stress tensor and fluid pressure. - *Journal of Geophysical Research*, *123*, 10, pp. 8748—8766.

DOI: http://doi.org/10.1029/2018JB016251

Journal of Geophysical Research: Solid Earth

RESEARCH ARTICLE
10.1029/2018JB016251

Moment Tensors of Induced Microearthquakes in The Geysers Geothermal Reservoir From Broadband Seismic Recordings: Implications for Faulting Regime, Stress Tensor, and Fluid Pressure

Changpeng Yu[1,2], **Václav Vavryčuk**[3], **Petra Adamová**[3], **and Marco Bohnhoff**[1,2]

[1]Section 4.2 Geomechanics and Rheology, GFZ German Research Centre for Geosciences, Potsdam, Germany, [2]Institute of Geological Sciences, Free University of Berlin, Berlin, Germany, [3]Institute of Geophysics, The Czech Academy of Sciences, Prague, Czech Republic

Key Points:
- Full moment tensors of 1,421 microearthquakes are calculated from broadband recordings to analyze the characteristics of source properties
- Significant spatial variations of faulting regime are observed and correlate with stress change due to fluid injection or regional tectonics
- Isotropic components of moment tensors reflect changes in downhole pressure due to fluid injection, migration, and extraction

Supporting Information:
- Supporting Information S1

Correspondence to:
C. Yu,
changpeng.yu@gfz-potsdam.de

Citation:
Yu, C., Vavryčuk, V., Adamová, P., & Bohnhoff, M. (2018). Moment tensors of induced microearthquakes in The Geysers geothermal reservoir from broadband seismic recordings: Implications for faulting regime, stress tensor, and fluid pressure. *Journal of Geophysical Research: Solid Earth*, *123*, 8748–8766. https://doi.org/10.1029/2018JB016251

Received 20 JUN 2018
Accepted 7 SEP 2018
Accepted article online 13 SEP 2018
Published online 4 OCT 2018

Abstract Full moment tensors of 1,421 microearthquakes in The Geysers geothermal field were calculated using waveform data from a field-wide broadband network and the approach based on the principal component analysis. Spatial characteristics of faulting regime, stress tensor and the isotropic component (ISO) of moment tensors were investigated. The studied events form different clusters dominated by normal faults (NF) and strike-slip (SS) faults, respectively. The SS-dominated clusters are related to the SS stress state observed in the southwestern side of the field where two NW-SE trending fault zones exist. Increasing proportions of SS faults were observed near the shallow and deep parts of the NF-dominated clusters. Temperature differences between the upper and lower parts of the reservoir do not change the overall stress states of clusters. The stress ratios in the NW part are much smaller than in the SE part of the field. The retrieved ISOs range between −5% and 25% for 96% of events. The average percentages of positive ISOs are correlated with the average injection rates in different clusters, and keep an increasing trend with depth below the main injection interval. Only 10% of events show negative ISO and are mainly constrained within the depth range of steam extraction. The proportion of events with negative ISO suggests much weaker seismic responses of the steam extraction than the water injection. The spatial variations of the ISO percentage do not follow the seismicity variations as the ISO is more sensitive to the pressure changes related to the fluid injection and migration.

1. Introduction

Since production at The Geysers geothermal field started in the 1960s, the water injection into the reservoir significantly enhanced the local seismicity rate (Beall et al., 2010; Majer & Peterson, 2007). The injection-induced seismicity temporally follows the long-term and short-term variations of the field-wide injection. The mechanisms of induced microearthquakes in The Geysers have been investigated by theoretical modeling (e.g., Segall & Fitzgerald, 1998), Thermal-Hydraulic-Mechanical numerical modeling (e.g., Rutqvist et al., 2016), and by field observations (e.g., Kwiatek et al., 2015; Martínez-Garzón et al., 2014), indicating effects of thermoelastic stress perturbation and pore pressure change on different temporal and spatial scales due to injection of cool water into highly fractured, hot reservoir. Thermal effects seem to dominate the release of the major seismic energy, whereas small but sufficient pore pressure changes (on the order of 1 MPa) result in rapid and far responses of microseismicity (e.g., Martínez-Garzón et al., 2013, 2014). These two types of stress changes may cause a discrepancy between spatiotemporal variations of the induced seismicity and the source characteristics (e.g., faulting regimes and isotropic components [ISOs] of seismic moment tensors [MTs]).

Investigations of the source characteristics and their spatiotemporal variations related to injection operations, reservoir properties, and regional tectonics are important for understanding the controlling factors of induced microearthquakes in a geothermal system. Although the early studies of source mechanisms in The Geysers were limited by network geometry at that time as well as instruments and analyzing techniques, the regional stress dominating over the local stress perturbations and the existence of significant non-double-couple (non-DC) mechanisms were observed already then (Julian et al., 1993; O'Connell & Johnson, 1988; Oppenheimer, 1986; Ross et al., 1996, 1999). A permanent network of ~30 short-period

stations (4.5 Hz), operated by the Lawrence Berkeley National Laboratory since 2003, significantly increased the ability of detecting induced events in The Geysers (Dellinger et al., 2017; Majer & Peterson, 2007). Waveform data and microearthquake catalogs of high quality are archived in the Northern California Earthquake Data Center (NCEDC) and remarkably promote the studies of induced seismicity in The Geysers.

Several studies focusing on the source mechanisms of small groups of events (15–53 events) of larger magnitudes ($M > 3.0$) and/or with limited spatial distributions were reported using either local short-period or regional broadband networks (Boyd et al., 2015; Guilhem et al., 2014; L. R. Johnson, 2014a, 2014b). The results from the full-waveform MT inversion in time and frequency domains and the first-motion inversion were compared. Source mechanisms showed complex source processes, indicating both shear and tensile failures. Significant isotropic parts of the MTs were observed, which deviated from other Northern California seismicity. A source model combining a shear crack and extended wing cracks was proposed to explain the increase in the ISO of microearthquake sources (L. R. Johnson, 2014b). However, as the data sets were of a limited size, no significant statistical and spatiotemporal characteristics related to injection operations could be observed.

At the same time, a particular cluster around injection wells Prati-9 and Prati-29 in the NW Geysers was studied based on a refined focal mechanism catalog (1,275 events) and a full MT catalog (869 events), which covered a time period between 2007 and 2014 (Kwiatek et al., 2015; Martínez-Garzón et al., 2016, 2017, 2014). The spatiotemporal variations of dominant normal and strike-slip faulting regimes with depth and with different injection stages were observed, which reflected the stress changes due to increased pore pressure and the corresponding changes in poroelastic stress. The occurrence and source characteristics of induced seismicity were influenced by both thermoelastic and poroelastic effects related to fluid injection and migration, with the thermoelastic effect dominating near injection well and poroelastic stress dominating at relatively far distance (Martínez-Garzón et al., 2014). The ISOs were temporally correlated with the injection rate and showed higher values near the injection wells, suggesting a pore pressure influence (Martínez-Garzón et al., 2017).

Other studies focused on the EGS Demonstration Project (Garcia et al., 2016) around the injection well Prati-32 in the NW Geysers. The stress tensor and finite-source parameters were calculated based on a MT catalog of 168 events obtained by the full-waveform inversion (Dreger et al., 2017, 2018; Gritto et al., 2016). Similar temporal rotations of the principal stresses and the corresponding variations of faulting regimes were observed as in other studies. In addition, the comprehensive Thermal-Hydraulic-Mechanical numerical modeling was performed to investigate the geomechanical effects of the cool water injection, including the mechanisms of the induced seismicity (Rutqvist et al., 2016), the observed stress rotations (Jeanne, Rutqvist, Dobson, et al., 2015), and seismic and aseismic deformations around the injection wells (Jeanne, Rutqvist, Rinaldi, et al., 2015).

The motivations of this study originate in three aspects. (1) The source mechanisms presented in the aforementioned studies are mostly based on recordings of short-period stations. Although the low-frequency components in short-period data can be roughly recovered by removing instrument response, such processing is unstable and significantly increases instrumental noise. In the broadband data, the low-frequency components are originally recorded, which allow us to extract more accurate *P* wave amplitudes in a broader frequency range. (2) The MT inversion based on the principal component analysis (PCA) was recently developed and successfully applied to microearthquakes (Vavryčuk et al., 2017). The robustness and high computational efficiency of the method make it feasible to create a large and reliable MT catalog using microseismic data with a rather low signal-to-noise (S/N) ratio and with complex waveforms. (3) Only a few field-wide investigations of source mechanisms in The Geysers were reported in recent years. The spatial variations of source mechanisms may reveal more details of the influence of fluid injection and regional tectonics on the seismicity.

In this study, we analyze spatial characteristics of source mechanisms derived from a new MT catalog that covers the whole area of The Geysers for a 1-year period. First, we introduce the process of developing the MT catalog using the broadband data set and the PCA-based MT inversion. By taking advantage of the broad frequency range and the high computational efficiency of the method, the MT solutions are retrieved using the optimal frequency band and time window. Then, we perform an uncertainty analysis by adding random noise and perturbing the velocity model and event locations. The error limits are defined to select the events with stable MTs. The faulting regime, stress tensor, and the ISO of MTs are investigated both in the field-wide dimension and for individual seismic clusters. The relationships between the spatial characteristics of these parameters and the injection operation, reservoir properties, and the regional tectonics are discussed.

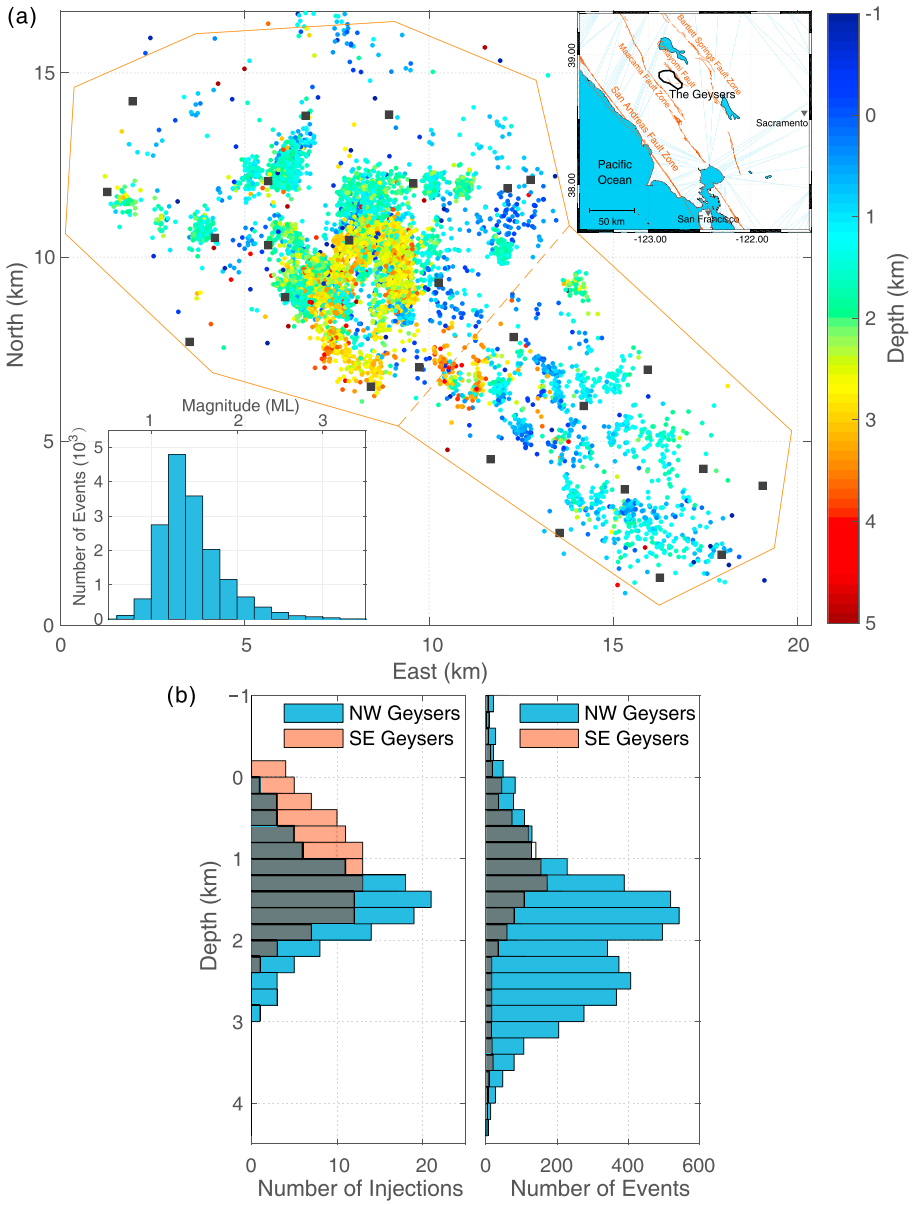

Figure 1. (a) Map of induced microearthquakes from June 2012 to June 2013 with $M_L \geq 1.5$ in The Geysers area. Event locations are from the double-difference catalog of the Northern California (Waldhauser, 2009). Solid squares denote the temporary network of 26 broadband seismic stations. (top right) Locations of The Geysers and the regional fault zones. (bottom left) Magnitude distribution of the double-difference catalog. (b) Depth distributions of the injection intervals along each borehole and the induced events shown in (a).

2. Study Area and Data

2.1. The Geysers Geothermal Field

The Geysers geothermal field is located between two right-lateral strike-slip faults, the Maacama Fault and the Collayami Fault, as part of the plate-bounding transform San Andreas Fault (SAF) system (Figure 1a). The orientation of local maximum horizontal stress (S_{Hmax}) is consistent with the NNE-SSW trending regional stress field (Boyle & Zoback, 2014; Martínez-Garzón et al., 2013; Oppenheimer, 1986; Provost & Houston, 2003). Despite that, the extension and strike-slip faulting regimes are different from the regional reverse and strike-slip background. Dominant NE striking fractures were observed in the shear wave splitting observations and fault plane solutions (Boyle & Zoback, 2014; Elkibbi et al., 2005; Lou et al., 1997). The Geyser

geothermal reservoir is vapor dominated and consists of the normal temperature reservoir (NTR) in the whole area and an underlying high temperature reservoir (HTR) in the northwest (NW) area (Beall & Wright, 2010; Stark, 2003). The temperatures in the NTR are approximately 240 °C and in the HTR can exceed 360 °C. The reservoir is highly fractured metagraywacke bounded by low permeability caprock and the granitic intrusions (Hartline et al., 2016).

The Geysers area can be divided into NW and SE parts as outlined in Figure 1a, by considering differences in seismicity rates, reservoir characteristics, injection operations, and seismic station configurations. There were 58 active injection wells and about 320 production wells during 2012–2013 when the temporal broadband seismic network was operating. The main injection interval (≥10 injections) is at about 1- to 2-km depth below the sea level in the NW area and at 0.5- to 1.7-km depth in the SE area (Figure 1b). The induced seismic events in the NW Geysers show a bimodal distribution along depth corresponding to the NTR (approximately 1–2 km) and the underlying HTR (approximately 2–3 km). The induced seismicity in the HTR is below the injection interval and results from the downward migration of fluids in the subhydrostatic reservoir of The Geysers (C. W. Johnson et al., 2016). The induced events in the SE area are fewer in number than in the NW area and mainly lie in a shallower NTR.

2.2. Data

The waveform data analyzed in this study were recorded by a field-wide surface network of 26 broadband seismic stations (Figure 1a), deployed under the GEISER project, and fully operated between June 2012 and July 2013 (Jousset et al., 2013; Zang et al., 2014). The network was equipped by Guralp (60 s-100 Hz) and Trillium (120 s-100 Hz) sensors, both of which have flat response curves within the valid frequency bands. Such high-density and wide-azimuth coverage of broadband stations are unprecedented and provide an opportunity to study the source mechanisms in much broader frequency band and at higher sensitivity level than before. The spectral analysis shows that the main noise components are the ocean-generated noise around 0.16 Hz and anthropogenic noise around 10–20 Hz (see supporting information Figure S1).

In addition, a permanent network of 31 short-period stations (4.5 Hz) is operated in this area since 2003 (Majer & Peterson, 2007). The broadband stations were collocated with selected short-period stations. Such configuration simplifies the basic processing (e.g., detecting, picking, and locating events) of the broadband data set by using the existing catalogs derived from the short-period data set. Three different earthquake catalogs based on the short-period data set in The Geysers are hosted by the NCEDC, including the NCSN catalog produced by the NCEDC, the relocated NCSN catalog (DD-NCSN) using the double-differences method (Waldhauser, 2009; Waldhauser & Schaff, 2008), and the EGS catalog produced by the Lawrence Berkeley National Laboratory (Dellinger et al., 2017). The three catalogs display systematic shifts in depth of events (~1 km). This has led to discrepancies in different studies when the absolute depth is needed to describe the relations between the reservoir seismicity and injection wells. In this study, the event locations of the DD-NCSN catalog showing the best focused clustering and a tight relation of seismicity with injection wells are used. The event depths are calibrated to the geoid (sea level) as in the NCSN catalog.

The magnitude distribution of the DD-NCSN catalog for the time period between June 2012 and June 2013 is plotted in Figure 1. Events with ML ≥ 2.0 (~1,421 events) are used to calculate the MTs. The *P* wave onset times are picked using the Suspension Bridge Picking (SBPx) algorithm (see the acknowledgments section). For the 1,421 events, a total number of 33,723 *P* wave phases is available in the records of the broadband data set. After removing the traces with anomalous amplitudes and with a low S/N ratio, 30,782 *P* wave phases (~91%) are used for calculating MTs. The same 1-D velocity model (Eberhart-Phillips & Oppenheimer, 1984) as used in the NCSN and DD-NCSN catalogs is utilized for calculating the Green's functions.

3. Methodology

Calculating accurate MTs of microearthquakes is challenged by a large number of events, complex waveforms, and a relatively low S/N ratio. To address these issues, a PCA-based MT inversion was developed to estimate the MTs of large microseismic data sets (Vavryčuk et al., 2017). The key step in this

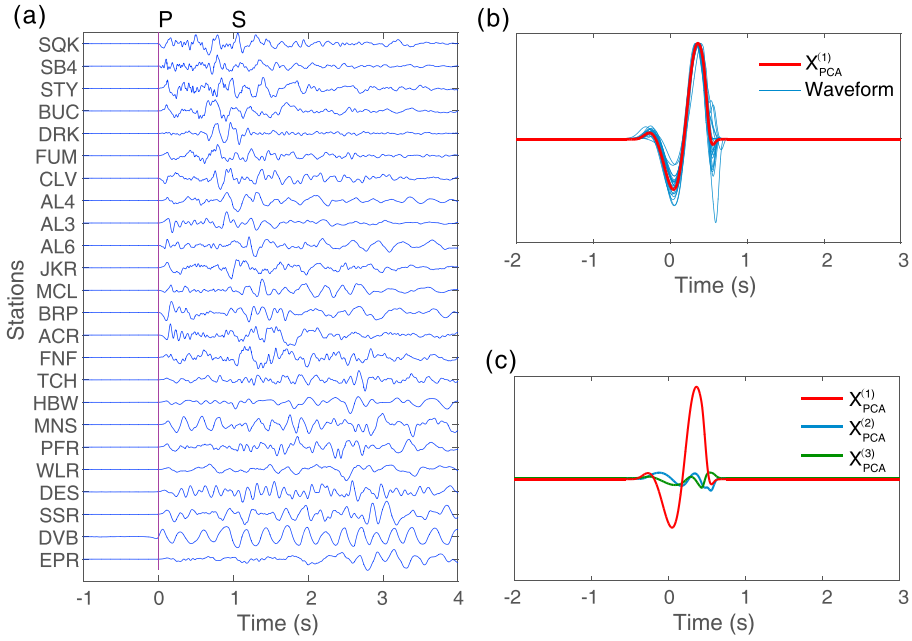

Figure 2. (a) Normalized vertical displacement waveforms of Event 71942345 (ML 2.68, depth 2.65 km). The traces are aligned with the *P* wave onset and sorted by hypocenter distances. (b) *P* waveforms after band-pass filtering (0.8–2 Hz) and windowing together with the first principal component. The polarities of the waveforms are flipped according to the first principal component. (c) Comparison of the first three principal components. PCA = principal component analysis.

approach is to automatically calculate the effective *P* wave amplitudes using the PCA. The MT inversions are usually based on the assumption that the point seismic source radiates direct waves with a common source wavelet into all directions. However, the source wavelet can be distorted by source directivity, multiarrivals, scattered waves, site effects, and other factors (see Figure 2a). While the *P* wave amplitudes directly picked in the original waveform data, either manually or automatically, contain rather high noise, the PCA analysis is capable of separating the common wavelet from the other interference signals and of reducing the errors in the measured amplitudes at individual stations.

The waveform data of an event form data matrix $\mathbf{X}$ with each column corresponding to one station. The PCA algorithm maps the data matrix $\mathbf{X}$ into an orthogonal space and produces a new matrix $\mathbf{X}_{PCA}$ of the same dimensions,

$$\mathbf{X}_{PCA} = \mathbf{XW}, \tag{1}$$

where the columns of matrix $\mathbf{W}$ (called *loading* in the PCA terminology) are the eigenvectors of the covariance matrix $\mathbf{X}^T\mathbf{X}$. In the orthogonal space, the columns of $\mathbf{X}_{PCA}$ represent independent waveform components of the original data matrix $\mathbf{X}$ that have different correlations between all the stations and are sorted according to the variances (magnitudes) of each component. If the common source wavelet dominates the waveforms, it is expressed as the first principal component $\mathbf{X}^{(1)}_{PCA}$ with the largest variance (Figure 2c). By reversing equation (1), the common source components at individual stations are then expressed as

$$\mathbf{X}_{Source} = \mathbf{X}^{(1)}{}_{PCA}\mathbf{W}_{(1)}{}^{T}, \tag{2}$$

where the elements of vector $\mathbf{W_{(1)}}$ reflect the weights of the common wavelet at individual stations and therefore can be used as the effective amplitudes. The signs of the elements in $\mathbf{W}_{(1)}$ indicate the polarities. The full MT solution is then calculated using the standard least squares inversion (see Vavryčuk et al., 2017). The retrieved MT solutions are further refined by calibrating the network to suppress the local effects (Davi & Vavryčuk, 2012). The reliability of the MTs is evaluated by the RMS defined as the normalized root-

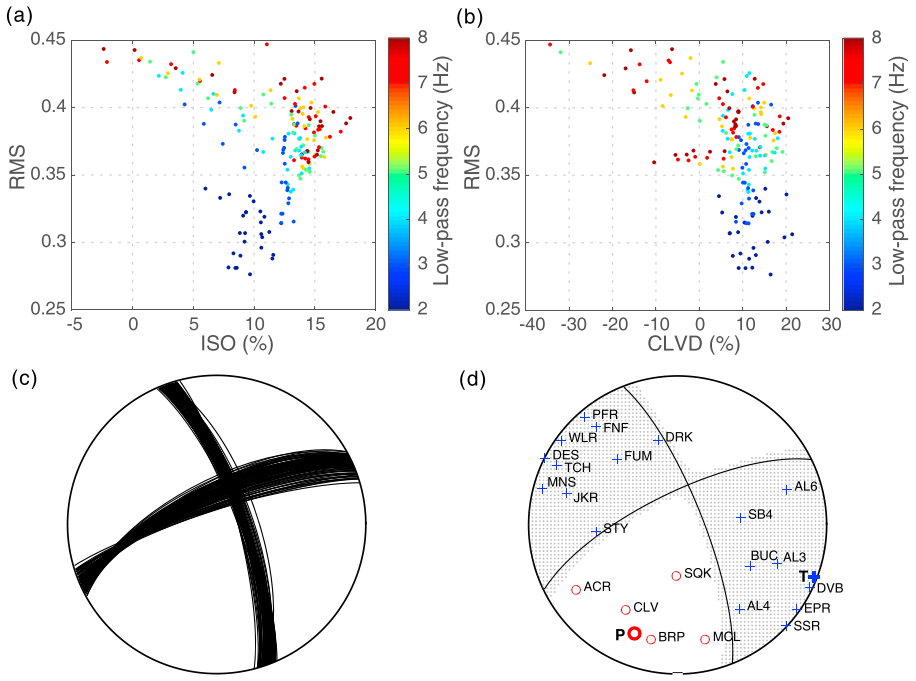

Figure 3. (a) ISO and (b) CLVD components of 182 candidate MTs plotted against the RMS for the Event 71942345 (ML 2.68). Seven groups of solutions with different low-pass frequencies (2, 3, …, 8 Hz) are color coded. In each group, 26 solutions are calculated using two high-pass frequencies (0.4, 0.8 Hz) and 13 time windows. (c) DC component of the 182 candidate MTs plotted as nodal planes in the focal sphere. (d) The optimal MT corresponding to the candidate solution with the lowest RMS in (a) and (b). The bold red circle/blue plus sign in (d) marks the *P*/*T* axis. The stations in (d) with red circles have a negative *P* wave polarity and with blue plus signs have a positive *P* wave polarity. The lower hemisphere equal-area projection is used in (c) and (d).

mean-square differences between the synthetic and observed amplitudes (see Vavryčuk et al., 2017). The final MTs are decomposed into the double-couple (DC), compensated linear vector dipole (CLVD), and ISO components (Vavryčuk, 2015). The relative percentages of three source components are calculated according to equation 8 in Vavryčuk (2001).

The performance of the PCA method depends on the degree to which the common source wavelet dominates the waveform data. Thus, to improve the efficiency of the PCA method, it is desirable to apply the band-pass filtering and windowing before the PCA procedure to suppress the site-dependent signals and to enhance the similarity of waveforms (see Figure 2b). Especially in The Geysers, the majority of events occur at shallow depths (approximately $\leq$ 3.5 km, see Figure 1) and the mountainous terrain (approximately elevations of 0.5–1.4 km) results in complex waveforms due to near-surface heterogeneities (see Figure 2a). Therefore, it is crucial to suppress these interference signals using carefully defined filters and time windows.

The high computational efficiency of the PCA-based MT inversion allows to perform a rather dense grid search for the optimal filter and time window. For each event, a total of 182 candidate MTs is calculated using 14 band-pass filters and 13 time windows. Being benefited from the broadband data set, the optimal band-pass filters for more than 70% of events in this study are determined to be from 0.4 or 0.8 Hz to 2 or 3 Hz, where the wavefield is less sensitive to site-dependent effects, to inaccuracies in the velocity model and to the attenuation (Q-factor). All the candidate MTs for one selected event are presented in Figure 3. The DC components expressed as nodal planes in the focal sphere show consistent geometry, while the RMS and the percentages of ISO and CLVD components vary widely against different frequency bands and time windows. It suggests that less optimal frequency band and time window introduce more uncertainties in the non-DC than in the DC components and result in a higher RMS. The optimal MT can be picked from a group of candidate solutions (e.g., 10 solutions) with the lowest average RMS and variances of the non-DC components or calculated by averaging the MTs of this group solutions.

Table 1
Error Limits of the P/T Axes and the Percentages of the CLVD and ISO Components for Noisy Data, Perturbations of the Velocity Model, and for Mislocation of Events

	Noise (±10%)		Velocity (±5%)		Location (95% confidence)	
	95% confidence	90% confidence	95% confidence	90% confidence	95% confidence	90% confidence
P axis (°)	2.91	2.15	2.64	1.64	3.00	2.04
T axis (°)	2.48	1.89	2.10	1.18	2.54	1.59
CLVD (%)	7.53	6.22	5.56	3.52	6.06	4.22
ISO (%)	1.97	1.50	1.53	0.91	1.96	1.16

The DC parts of the retrieved MTs were used for classifying the faulting regimes and for calculating the stress tensors. The faulting regimes are classified based on the plunge angle δ of the *P*/*T*/*B* axes (Frohlich, 2001). The relative weights of strike-slip, normal, and thrust faults are expressed as $W_{SS} + W_{NF} + W_{TF} = \sin^2\delta_B + \sin^2\delta_P + \sin^2\delta_T = 1$. The stress tensors are calculated using the modification of Michael's method (Michael, 1984) proposed by Vavryčuk (2014). The method inverts jointly for stress and fault orientations by applying the fault instability criterion (Vavryčuk, 2011a). The method runs in iterations and numerical tests show that it is fast, accurate, and performs better than the standard linear inversion. To perform the calculation, we use the open access Matlab code STRESSINVERSE (Vavryčuk, 2014). The non-DC parts of the retrieved MTs were used to classify the source types that were plotted in Hudson's diagram (Hudson et al., 1989; Vavryčuk, 2015).

4. Results

4.1. Uncertainty Analysis

To access the uncertainties of the MTs originated from noise in waveform data, an inaccurate velocity model and inaccurate locations, multiple inversions are performed by adding to amplitudes random noise up to 10% level and considering the 5% velocity perturbations and the location errors at the 95% confidence level in the calculation of Green's functions. Perturbations of the velocity model and of locations affected geometry of rays, geometrical spreading, and conversion coefficients at the Earth's surface. The error limits of all the MTs are statistically calculated in terms of the *P*/*T* axes for the DC part and the percentages of the CLVD and ISO for the non-DC part (Table 1). In both DC and non-DC parts, the influences of amplitude noise and the mislocation are larger than the inaccuracies in the velocity model under given perturbation levels. The error limits of the *P*/*T* axes at the 95% confidence level are lower than 3° in all three cases, which means that the fault plane solutions are very stable. Nevertheless, the orientations of the *P* axis show higher error limits than the *T* axis, as there is a transition of the maximum principal stress between the horizontal and vertical directions corresponding to normal and strike-slip faulting in this region. The uncertainties of the CLVD component are much higher than that of the ISO, because the CLVD is more sensitive to errors in the inversion than the ISO. This observation is consistent with the results in other areas (Stierle, Bohnhoff, & Vavryčuk, 2014; Stierle, Vavryčuk, et al., 2014; Vavryčuk, 2011b). The error limits of the ISO at the 95% confidence level are less than 2% in all three cases and are much lower than the spatial and temporal variations of the ISO as well. It suggests that the ISOs are stable and reliable to be interpreted. The error limits presented in Table 1 are used as the criteria to select stable events for interpretations of the DC and non-DC components.

The accuracy of the MTs strongly depends on the network configuration controlled by the number of stations and by the coverage of stations on the focal sphere. In comparison with the NW Geysers, the network configuration in the SE Geysers is relatively poor and the events are much shallower (Figure 1). Both these factors have negative effects on the MTs and result in a higher RMS (Figure 4) and in higher uncertainties in DC and non-DC components. In addition, the total number of events in the SE Geysers is only 24% of that in the NW Geysers (Figure 1b). Using the same criterion (e.g., the errors limits of *P*/*T* axes at the 95% confidence level), 91% of the events in the NW Geysers are selected as stable events, while in the SE Geysers the proportion is only 73%. As a consequence, the interpretations of MTs in the SE Geysers are more limited, especially for the non-DC components.

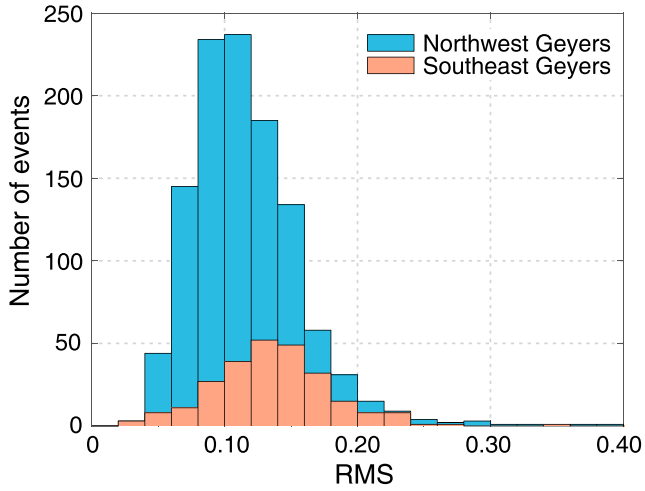

Figure 4. RMS distributions of the moment tensors in the NW and SE Geysers.

Constrained MT inversion only for the deviatoric components is also performed to evaluate the improvement of the full MT inversion. If the ISO is considered, the average RMS of the entire catalog decreases from 0.21 to 0.12, which is reduced by about 42%, and the variance reduction defined as (1-RMS)*100 increases from 79 to 88.

4.2. Faulting Regimes and Stress States

The DC component of the MTs, usually presented as the fault plane solution, represents the most common mechanisms of earthquakes (i.e., the shear faulting model). The fault plane solution is equivalently described by the fault normal and slipping directions, or by strike, dip and rake angles, or by the *P* (pressure), *T* (tension), and *B* (neutral) axes. In this study, the fault plane solutions are presented by the *P*/*T*/*B* axes, because their configurations can intuitively reflect the stress directions. Moreover, the faulting regimes can be easily classified according to the plunge angles of the *P*, *T*, and *B* axes.

Although the uncertainty analysis indicates that fault plane solutions are of high accuracy, the error limits of the *P*/*T* axes at the 95% confidence levels defined in Table 1 are used to further select events with stable solutions. Hence 1,192 events are selected from the total of 1,421 events and their *P*/*T* axes are projected in the lower hemisphere (Figures 5a and 5b). The SE Geysers region is characterized by fewer events and by a higher RMS as well as more scattered *P*/*T* axes than the NW part of The Geysers field. The orientations of the *T* axes show stable clusters near the horizontal direction and around two prominent symmetric azimuths (N71°W and N109°E). The orientations

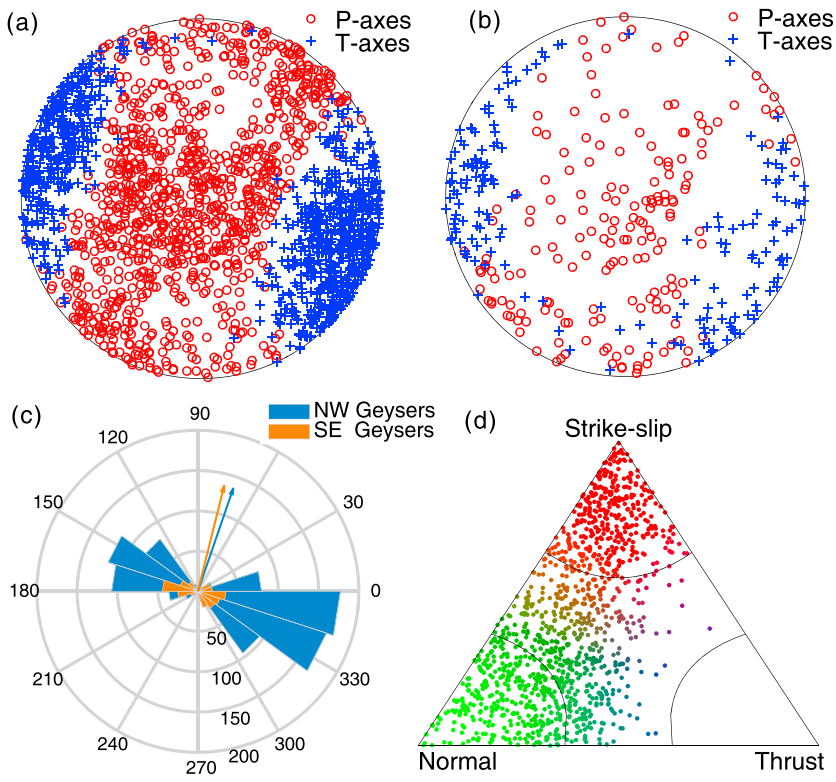

Figure 5. *P*/*T* axes of 1,192 selected events with stable solutions in (a) the NW and (b) the SE Geysers. The lower hemisphere equal-area projection is used in (a) and (b). (c) Azimuth distributions of the *T* axis, and the retrieved directions of the S_{Hmax} (N19°E in the NW and N14°E in the SE Geysers). (d) Faulting regimes classified by the plunge angles of the *P*/*T*/*B* axes (Frohlich, 2001). The RGB color map is used in (d) to represent the relative weights of normal/strike-slip/thrust faulting in each event. The contours in (d) correspond to 30° of the *P*/*T*/*B* axes off the vertical direction.

of the *P* axes can roughly be separated into two groups around the vertical and horizontal directions, respectively. Such configuration of *P*/*T* axes typically represents normal and strike-slip faulting regimes. Thrust faults are observed only very exceptionally in the stable events. According to Anderson's classification scheme (Zoback, 2007), the normal/strike-slip faulting regimes suggest a stress state of $S_V \approx S_{Hmax} > S_{Hmin}$. The maximum principal stresses vary between the horizontal and vertical directions, resulting in a transition between the strike-slip and normal faults. The preferred azimuths of the *T* axes correspond to the direction of S_{Hmin}. The azimuths of S_{Hmax} perpendicular to S_{Hmin} are N19°E and N14°E for the NW and SE Geysers (Figure 5c), respectively. Such a slight rotation is not significant considering the error limits of the *T* axes and therefore may originate from higher uncertainties due to poor station coverage in the SE Geysers. The azimuths of the S_{Hmax} and S_{Hmin} are consistent with the results of the stress inversions in this area (see below).

The ternary distribution illustrates variations of faulting regimes in the domain of normal/strike-slip modes (Figure 5d). Some events show mixed features of normal and strike-slip faults. The RGB color map is used to code the relative weights of the normal/strike-slip/thrust faults ($W_{SS}/W_{NF}/W_{TF}$) in individual events. To better understand the spatial characteristics of faulting regime, the color-coded faulting regimes are further projected into the map and profiles (Figure 6). In addition, 12 clusters of events are analyzed in particular. These clusters are identified in the 3-D map according to the local event density and the spatial correlations between events and injection wells. The cluster edges are carefully defined to include the events most possibly related to the neighboring injection wells and to exclude the events that are more scattered and are difficult to be assigned to specific injection wells. Each cluster is in response to only a few injection wells within it ($\leq$ 3 wells), except for clusters C11 and C12 in the SE Geysers, where the events with stable solutions are too sparse. Such way of event clustering is not perfect, but it does capture the most prominent features that are related to the injection behavior.

For the whole area, a visible dominance of the normal faults ($W_{NF} > 50\%$) over the strike-slip faults ($W_{SS} > 50\%$) is observed in map and section views. Statistically, the normal faults are by 25% more frequent than the strike-slip faults, suggesting a more extensional tectonics in this region. However, five clusters (C6, C11, C3, C4, and C8) with much larger proportions of the strike-slip faults are distinct from the normal-faulting background (see Figures 6 and 7a). In section views, two major strike-slip-dominated clusters (C6 and C11) form clear high-angle trends extending to the deeper part of the reservoir. In the map view, C6 and C3 form a linear extension in parallel with the NW-SE trending strike-slip regional faults as part of the SAF system. It is natural to link these strike-slip-dominated clusters with some unmapped strike-slip faults controlled by the regional stress regime. The steep distributions of events in C6 and C11 might imply fluid migrations along the fault zones of high permeability. The distinct strike-slip faulting regime may be attributed to the regional strike-slip stress regime and the preexisting fractures around the unmapped faults. In addition, the faulting regimes in the SE Geysers are distinctly separated into two groups with almost all strike-slip and normal faults as shown in the clusters C11 and C12. A NW-SE trending boundary seems to exist between these two groups of events.

In spite of five clusters with predominant strike-slip faults, the rest of clusters are characterized by larger proportions of the normal faults. In five major normal-fault-dominated clusters (C7, C2, C1, C5, and C10), the relative proportions of the normal and strike-slip faults vary with depth (Figure 7b). In the clusters with the majority of events in the NTR (C1, C2, and C5), the proportion of the strike-slip faults increases as the events approach the bottoms of the clusters. C7 and C10 have much wider depth ranges with the majority of events in the HTR and the minority in the overlying NTR. The relative proportions of strike-slip faults in these clusters tend to be higher near the shallow and deep parts.

Spatial variations of faulting regimes reflect heterogeneities of the stress field or the distribution of preexisting fractures in the reservoir. Stress inversions are performed for the 12 clusters from different parts of the reservoir and with different faulting regimes. The principal stresses (σ_1, σ_2, and σ_3) and the stress ratio $R = (\sigma_1 - \sigma_2)/(\sigma_1 - \sigma_3)$ are derived for each cluster (Figure 8). Clusters C1, C2 and C7, C10 are four major clusters that are located in the NTR and HTR and dominated by normal faults. These four clusters show similar stress states with close orientations of the σ_1 axis near the vertical direction and the σ_2 and σ_3 axes near the horizontal directions. Such consistency of the stress states in the NTR and underlying HTR suggests no significant stress changes on the scale of clusters due to fluid injections and migrations or different

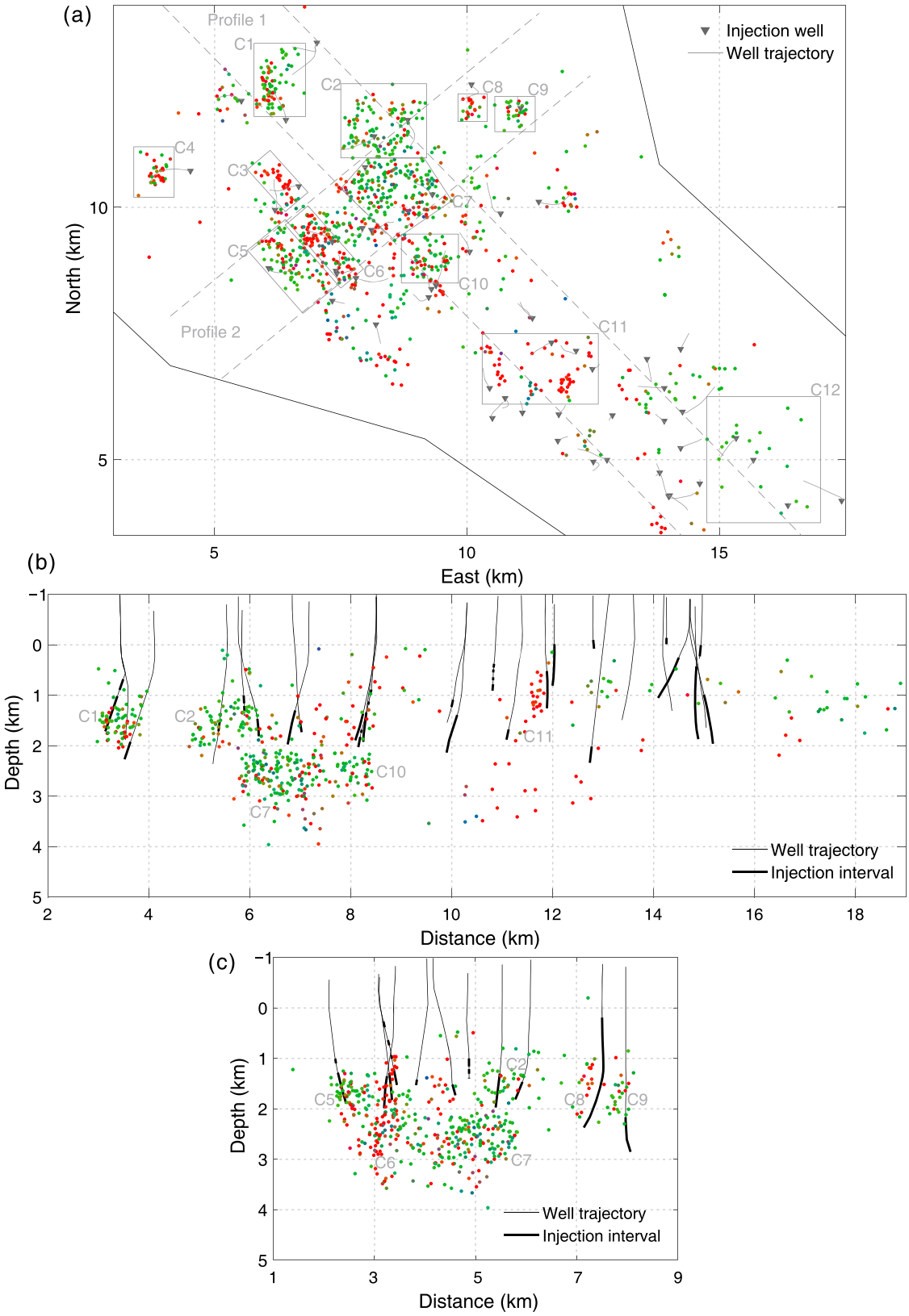

Figure 6. (a) Map view; (b) and (c) cross-section views of events with different faulting regimes color-coded as in Figure 5d. The dashed lines in (a) indicate the extents of Profiles 1 and 2 shown in (b) and (c). Twelve clusters are identified and marked in map and section views (see text for details). Since the events of different clusters overlap in the section views, the cluster edges are only plotted in the map view.

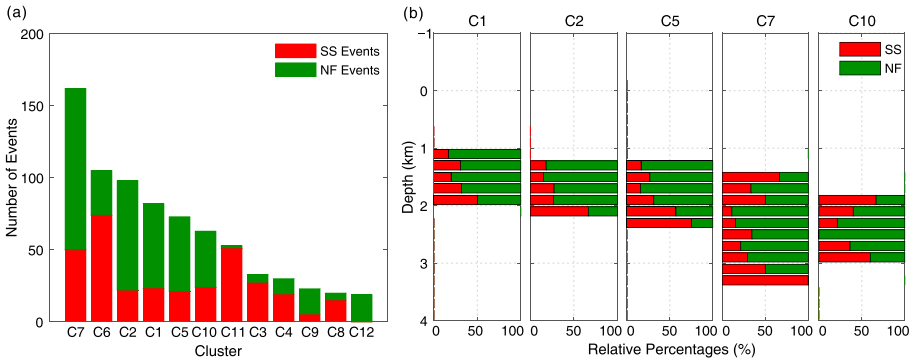

Figure 7. (a) The total number of events and the relative proportions of the normal ($W_{NF} > 50\%$) and strike-slip events ($W_{SS} > 50\%$) in the clusters marked in Figure 6. (b) The relative percentages of the normal and strike-slip faults along depth in clusters C1, C2, C5, C7, and C10. The thickness of the depth bins in (b) is 200 m. Only depth bins with five or more reliable moment tensor solutions are plotted. SS = strike-slip; NF = normal fault.

thermal properties. Nevertheless, the low stress ratios in these clusters indicate that the magnitudes of σ_1 and σ_2 are very close and a small external loading could rotate the directions of σ_1 and σ_2. Therefore, stress rotations on the suborder scale may occur due to external perturbations, for example, fluid injection and migrations. This explains the depth-dependent variations of relative proportions of the normal and strike-slip faults within the clusters as illustrated in Figure 7b. Clusters C3, C4, C5, C6, and C11 show more strike-slip stress regime with σ_1 tending to rotate toward the horizontal direction and σ_2 toward the vertical direction. Such strike-slip stress is consistent with the large proportions of strike-slip faults observed in clusters C3, C4, C6, and C11. The distinct stress states also support the interpretations of the linear trends and high-angle extensions of events in the map and profile of clusters C3, C6, and C11, which may be related to the strike-slip fault zone. Note that these five clusters are all located in the SW side of The Geysers area and close to two NW-SE trending fault zones as part of the regional tectonic system (see Figure 8). Thus, the distinct stress states and faulting regimes in these clusters may reflect the influences of the regional strike-slip stress regime. In addition, the rotations of S_{Hmax} and S_{Hmin} in counterclockwise direction are observed around the clusters C3, C4, and C5.

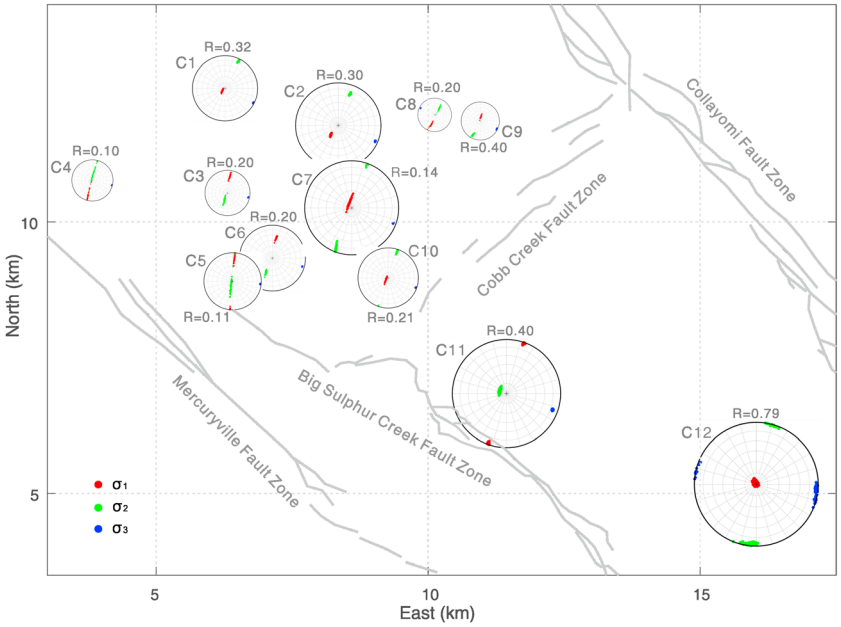

Figure 8. Confidence limits of the principal stress directions and the stress ratios (*R*-values) for the 12 clusters. The radius of the spheres with stress directions is scaled approximately according to the relative horizontal extents of each cluster. The map scale is the same as Figure 6a. The fault traces are from Dellinger et al. (2017).

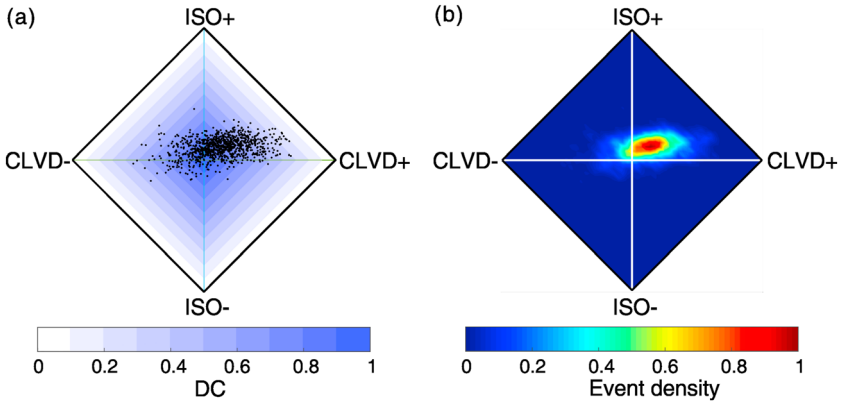

Figure 9. (a) Scatter and (b) normalized density source plots of the 984 selected events with reliable non-DC components. For the detailed description of the CLVD-ISO diamond plot, see Vavryčuk (2015).

Although the event densities in clusters C11 and C12 are not as high as in clusters of the NW Geysers, the stress inversions yield stable solutions that correspond to almost pure strike-slip and normal faulting in these two clusters, respectively. The stress ratio is much higher than that in the clusters of the NW Geysers, suggesting more stable stress states under the local perturbations caused by fluid injection. Although cluster C9 in the NW Geysers has a similar stress ratio as cluster C11, the number of events and the horizontal extent of C9 are much smaller than those of C11. Therefore, this exception cannot change the background of the low stress ratio in the NW Geysers field.

4.3. ISO of MTs

Non-DC components of MTs describe minor parts of the mechanisms of earthquakes, such as the tensile, volcanic, or deep earthquakes. The non-DC components are sensitive to the uncertainties in the MT inversion (e.g., noise in data, inaccurate velocity model, and event locations). In comparison with the DC component, the stricter criteria are applied to select reliable non-DC components. The error limits of the *P* and *T* axes at the 95% and 90% confidence levels and the error limits of the CLVD and ISO at the 95% confidence levels are used as the thresholds to select reliable events. In this way, we keep 984 (70%) of total 1,421 events with reliable non-DC solutions for the following analyses. The majority of the selected events show positive ISO and CLVD components which are correlated with each other (Figure 9). Such pattern in the source-type plot agrees with the theoretical modeling of the shear-tensile source mechanisms (Vavryčuk, 2011b, 2015) and indicates the influence of massive fluid injection in this area. Elastic anisotropy in the focal area can also result in significant spurious non-DC components for either pure shear or shear tensile faulting (Vavryčuk, 2005; Vavryčuk et al., 2008). However, the anisotropy-induced non-DC components have distinct patterns in the source-type plot, which do not match the observations shown in Figure 9 (see Figure 3 in Vavryčuk, 2015).

The statistical distributions of the DC, CLVD, and ISO percentages are presented in Figure 10. Almost 90% of events are characterized by the positive ISO and 75% by the positive CLVD. The ISOs in 96% of events range from −5% to 25%, while the CLVDs in 92% of events range from −20% to 50%. The significant amount of the positive non-DC components is closely associated with injection operations in this area. The ISO representing the volumetric changes in the source region can be directly related to the pressure change due to fluid injection. The interpretation of the CLVD is more difficult because the CLVD is rather sensitive to errors produced by the MT inversion (Vavryčuk, 2011b) and it might also reflect other source complexities such as irregular fault geometry. Nevertheless, the same signs of the ISO and CLVD usually indicate the shear-tensile faulting regime (Vavryčuk, 2011b, 2015).

The percentages of the ISO are projected into the map and profiles to illustrate their spatial variations (Figure 11). Because of the low seismicity and higher uncertainties introduced by poor station coverage and shallow foci, the events with reliable solutions in the SE Geysers are too sparse to form clear patterns for interpretation. Therefore, we focus on the NW Geysers that has higher event density and more reliable solutions. Ten clusters in the NW Geysers defined in the previous section are used to characterize the spatial variation of the ISO. Each cluster is directly in response to the injection wells within it ($\lesssim$ 3 wells).

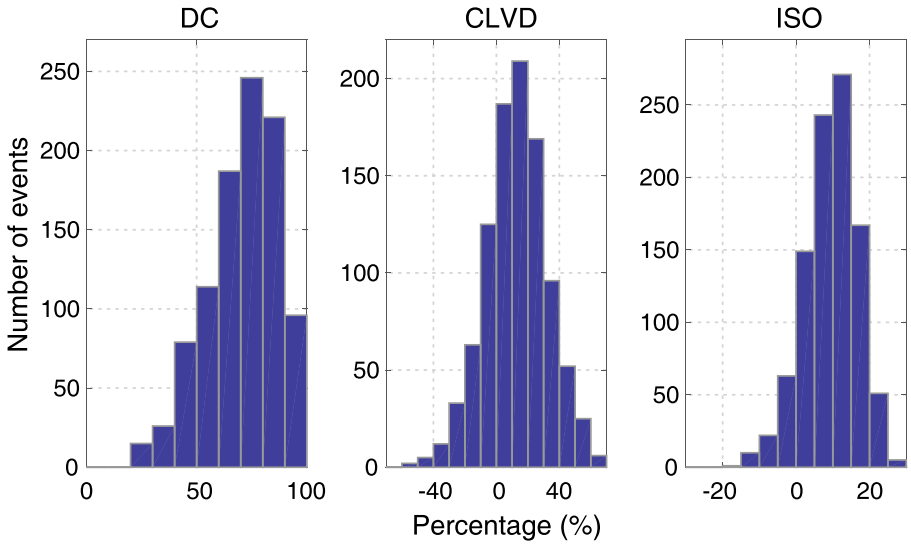

Figure 10. Statistical distributions of the DC, CLVD, and ISO percentages.

We compare the average percentages of positive ISOs, the number of injection wells, the average injection rates, the gross injection volume, and the number of events for the 10 clusters in the NW Geysers observed in the studied time period (Figure 12). In general, the injection rate of an individual well controls the initial pressure at the borehole and the average pressure level within the stimulated volume. In the clusters with multiple injection wells, the aggregate injection rates are obtained by summing all individual wells. Considering the local complexity of pressure diffusion, the aggregate injection rate cannot reflect the average pressure levels within the stimulated volume as precisely as in the clusters with a single injection well. Nevertheless, more injection wells within a limited area result in larger injection volume and higher average pressure level that have a potential to induce more volumetric changes in the source region. This explains the higher levels of ISO in the clusters (C6, C3, C7, C10, C1, and C2) with two or three injection wells that are characterized by larger average injection rates and gross injection volumes (Figure 12a). For the clusters with a single injection well and simple shapes of event clouds (C4, C5, C9, and C8), the average levels of positive ISOs are closely correlated with the average injection rates of individual wells, which further indicates a strong influence of pressure level on the ISO. In addition, clusters C6 and C3 showing the highest level of positive ISOs are characterized by the predominant strike-slip faults and interpreted to be related to fault zone. The higher permeability and the compliant elastic properties around the fault zone can also enhance the influence of pressure level on the volumetric changes in the source region.

It is also worth noting in Figure 12, especially for the clusters with a single injection well, that the number of events in different clusters are closely correlated with the gross injection volumes rather than with the average injection rates, and the average percentages of positive ISOs have a better correlation with the average injection rates although such correlation is not that obvious because of the *aggregate* injection rates in the cluster with multiple injection wells. The average percentages of positive ISOs have no correlation with the number of events in the clusters. It seems that the ISO is more sensitive and has stronger response to the pressure changes caused by fluid injection than the occurrence of induced seismicity.

Among the four clusters with the highest level of positive ISOs, the majority of the events in Clusters 6, 7, and 10 extend to the HTR at depth ~2–3 km underlying the NTR at depth of ~1–2 km. The rest of clusters with a relatively low level of ISO mainly lie in the NTR. This causes visible variations of ISO with depth along Profiles 1 and 2. To highlight the vertical variation of the ISO and understand its relation to fluid injection, we calculate the average percentages of positive ISOs within each depth bin of 200 m and compare with the numbers of events and active injection intervals at the same depth range (Figure 13). As indicated by the depth distribution of injection intervals, the fluid injections are mainly performed between 1 and 2 km that is the depth range of the NTR. Above the main injection interval, the number of events and the average percentage of positive ISOs both stay at low levels. As the number of injections increase with depth to the maximum level, the number of events increases rapidly and reaches its maximum. Meanwhile, the average percentage of

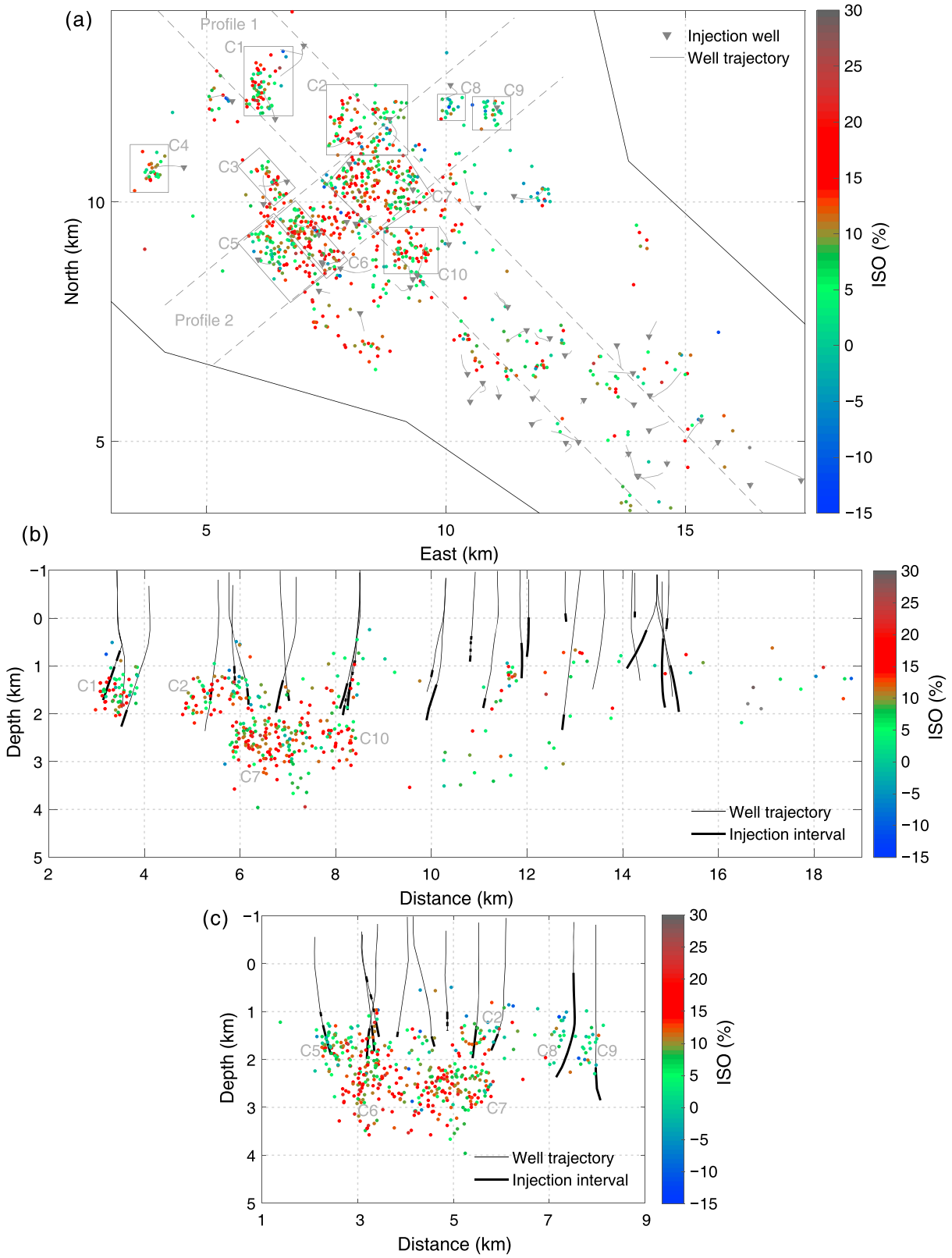

Figure 11. (a) Map view; (b) and (c) cross-section views of events with different percentages of the ISO. The dashed lines in (a) indicate the extents of Profiles 1 and 2 shown in (b) and (c). Ten clusters in the NW Geysers are marked in map and section views. Since the events of different clusters overlap in the section views, the cluster edges are only plotted in the map view.

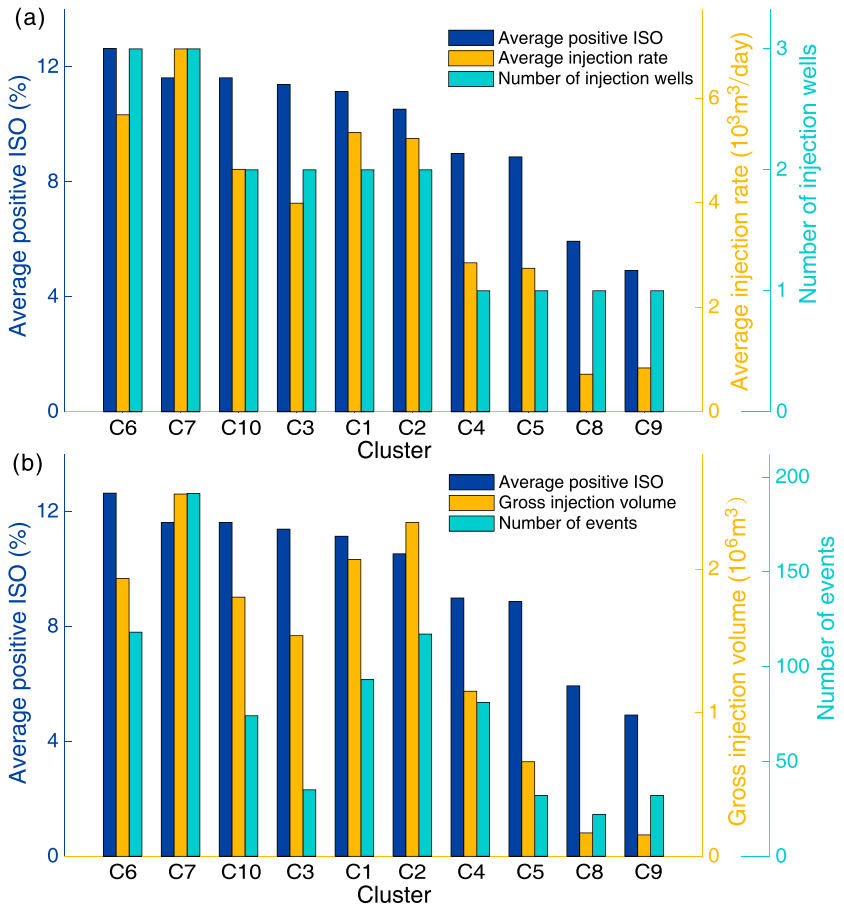

Figure 12. Comparisons of the average percentages of positive ISOs with (a) the number of injection wells, the average injection rates and (b) the gross injection volumes, the number of events (ML ≥ 2.0), for the studied time period and the clusters marked in Figure 11. The average injection rates and the gross injection volumes in the clusters with two or three injection wells are obtained by summing all the wells.

positive ISOs increases to a high level (~10%). After the injections reaching the maximum level in depth (~1.5 km), the number of events starts to decay, though there is a minor peak below the main injection interval due to the fluid migration into the HTR zone. Interestingly, the percentage of positive ISOs stably increases below the depth of the maximum injections until the depth, where the event number decreases to very low level (~3 km).

As stated above, the average percentage of the positive ISOs and the induced seismicity reach to relatively high levels in the main injection interval as a result of the rapid increase of injections with depth. The fluid injected in the main injection interval migrates into the HTR zone and induces events with a higher level of ISO. The continuous increase of the percentages of positive ISOs with depth below the main injection interval is intuitively related to the progressive increase of pore pressure along the downward migration of fluid. The discrepancy between the vertical variations of the positive ISOs and the number of induced events may suggest that the ISO is more sensitive to the pore pressure changes caused by fluid injection or migration, and the induced seismicity is additionally influenced by other factors.

In addition, the events with the negative ISOs are mainly constrained within the depth range of the NTR (Figure 13c), where large volumes of steam are extracted from the reservoir. This is consistent with the mechanism of negative ISOs that are explained to reflect the compaction of the source region. The events with positive ISO follow the bimodal distributions of induced events, which reflects the effects of both fluid injection and migration. Moreover, a large contrast in populations of positive and negative ISOs is observed, indicating that the seismic response of steam extraction is much weaker than the water injection.

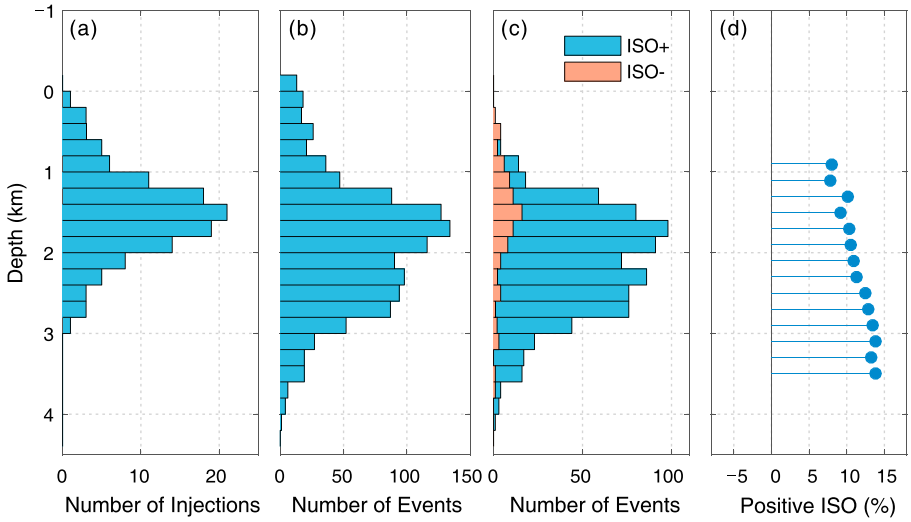

Figure 13. Depth distributions of (a) the injection intervals along each borehole, (b) the induced events (ML ≥ 2), and (c) the events with reliable positive or negative ISOs in the NW Geysers. (d) The average percentages of positive ISOs (at least five reliable values) within each depth bin of (a)–(c).

5. Discussion and Conclusions

Full MTs of a total of 1,421 selected earthquakes are derived from broadband waveform recordings of a 1-year field-wide network in the Geysers geothermal reservoir. The analyzed earthquakes cover the whole Geysers area and provide an opportunity to depict the spatial variations of faulting regimes, stress tensors and ISO components, and their relationships with injection operations throughout the reservoir. This work extends previous studies on induced seismicity in The Geysers that were obtained from short-period seismic stations, therefore allowing the earthquake-physical processes related to fluid injection based on a broader frequency band.

The studied microearthquakes are characterized by dominant normal and strike-slip faulting regimes. In total, the normal-faulting events are by 25% more frequent than the strike-slip events, suggesting a dominant extensional tectonic regime in this region. Such pattern is different from the reverse and strike-slip regional regimes controlled by the SAF system. The average azimuth of S_{Hmax} obtained in this study is N19°E, which is close to that reported by previous studies (N15°E in Martínez-Garzón et al., 2013; N26°E in Boyle & Zoback, 2014; N20°E in Dreger et al., 2018) and consistent with the orientation of the regional background stress (Provost & Houston, 2003). The stress inversion results show low stress ratios especially in the NW Geysers, which may result in rotations of the principal stresses σ_1 and σ_2 due to small stress perturbations (e.g., fluid injection and migration and fault zone) and cause lateral or depth-dependent variations of faulting regimes. The SE Geysers shows a simpler configuration of faulting regimes and more stable stress fields.

We identify distinct seismicity clusters with remarkably predominant strike-slip faulting mechanisms. These clusters of seismicity are characterized by the high-angle extension to the deeper part of the reservoir and by the NW-SE trending extension in parallel with the regional faults. This indicates the influence of fault zones controlled by the strike-slip tectonic regime of the SAF system, for example, the NW trending Big Sulphur Creek Fault Zone (see Sadowski et al., 2016; Thomas et al., 1986). Injected fluids can migrate downward along a fault zone of high permeability and induce more strike-slip events under the particular stress state. In the SE Geysers, the events are separated into two groups with almost pure strike-slip and normal faults and distinct stress states.

Depth-dependent variations of faulting regimes are observed within five major clusters with dominant normal-faulting mechanisms. The relative proportions of the strike-slip faults tend to be larger near the top and bottom of clusters confirming earlier results by Martínez-Garzón et al. (2013). Such depth-dependent variations of faulting regime only exist in those clusters with dominantly normal-faulting mechanisms. These

clusters are less influenced by the regional strike-slip stress and therefore are highlighted by the effects of fluid injection and production. In addition, the variations do not depend on the absolute depths but on the relative depths within each cluster. These details imply that such variations are closely related to the local fluid injections and migrations within each cluster. Numerical modeling of The Geyser geothermal reservoir performed by Jeanne, Rutqvist, Dobson, et al. (2015) shows that thermal cooling effects cause a decrease in vertical stress due to contraction and a relative increase of horizontal stress due to stress redistribution for an initial normal-faulting stress regime, above and below the cooling area. This leads to rotations of the σ_1 and σ_2 axes that may change the regime from normal faulting to strike-slip faulting.

The spatial variations of faulting regimes may arise from local variations of stress field and/or preexisting fracture sets. The results of the stress inversion indicate that four major clusters in the NTR and HTR show similar stress states. Such consistency suggests no significant changes of average stress in the NTR and HTR regardless of fluid injections, migrations, and different thermal contrasts. However, as the low stress ratios in these clusters indicate close magnitudes of σ_1 and σ_2, the suborder stress variations may occur due to external perturbations, for example, caused by fluid injection and migration. This explains the depth-dependent variations of relative proportions of normal and strike-slip faults within the clusters. Distinct strike-slip stress regime around the clusters with remarkably predominant strike-slip faults supports the interpretation that these clusters are influenced by the fault zones controlled by the regional tectonic stress. The stress inversion in the SE Geysers shows two distinct stress states with much higher stress ratios, which correspond to two groups of events with almost pure strike-slip and normal faults.

A significant level of positive ISOs is observed for the studied microearthquakes. The source-type plot shows a major shear-tensile mechanism. The percentages of the ISO obtained in this study show a stable distribution within a narrow range between −5% and 25% (96% of events). Only 10% of events display the negative ISOs. The positive/negative ISOs probably have direct links with pore pressure changes due to fluid injection and extraction in the reservoir.

The comparisons of the average percentages of positive ISOs and the injection parameters in different clusters indicate a spatial correlation of the positive ISO with the average injection rate that controls the average pressure level within the stimulated volume, rather than with the gross injection volume. Statistical analysis at different depth intervals indicates that the percentage of positive ISOs is controlled not only by the rapid increase of the pressure level in the main injection interval but also by a progressive increase of pressure along the downward migration of fluids below the main injection interval. Fluid migration into the HTR has been evidenced by the migration of the induced seismicity below the NTR (C. W. Johnson et al., 2016; Stark, 2003). The accumulating effects along with the fluid migration in the downward direction cause a progressive increase of pore pressure level, which results in the continuous increase of the percentage of positive ISOs with depth below the main injection interval.

The spatial variations of the average level of positive ISOs do not coincide with the event-density distribution of induced seismicity in this area. The higher levels of ISO are not always accompanied with a higher occurrence of seismicity. The seismicity is more closely correlated with the gross injection volumes, whereas the average level of positive ISOs is correlated with the average injection rates. Such effect can be explained by different controlling factors of the ISO and of the occurrence of the seismicity. The ISO seems to be more sensitive to the pressure changes related to fluid injection or migration and shows more straightforward and stronger response. The seismicity is primarily induced by the thermoelastic stress perturbation around the preexisting fractures and simultaneously controlled by the pore pressure change at relative farther distance (Kwiatek et al., 2015; Martínez-Garzón et al., 2014; Rutqvist et al., 2016; Segall & Fitzgerald, 1998). The discrepancy between the positive ISO and the induced seismicity cannot be observed in temporal variations as they both show correlations with the injection rate temporally.

The events with the negative ISO show distinct depth distribution, which corresponds to the depth range of the steam extraction. The negative ISO can thus be interpreted as a result of a compaction of the medium due to the steam extraction. A large contrast in populations of positive and negative ISOs suggests that the seismic response of the steam extraction is much weaker than the water injection. In The Geysers area, the total number of injection wells is far less than that of the production wells (e.g., 58 active injection wells and more than 320 production wells in this study). The water injection into tens of wells causes much stronger local perturbations of thermoelastic and poroelastic stress resulting in the microseismicity. After vaporization and

migration, such stress perturbations are diffuse and spread out into the reservoir. As the steam is extracted from hundreds of production wells over the field, the local effects (pressure decline and heat extraction) would not be as stronger as in injection operations.

Acknowledgments
The work was supported by the German Research Foundation (grant number Bo1877/10-1) and the Grant Agency of the Czech Republic (grant 16-19751J). We thank Grzegorz Kwiatek, Patricia Martínez-Garzón, Philippe Jousset, and Eva Stierle for helping with the processing of the raw data set and the interpretations of the results. The analyzed waveforms are available from the authors upon request (section 4.2 of GFZ Potsdam, changpeng.yu@gfz-potsdam.de). The seismic event catalogs were accessed through the Northern California Earthquake Data Center (NCEDC, http://www.ncedc.org/). The information of injection wells, injection, and production operations were collected from the California Department of Conservation, Division of Oil, Gas, & Geothermal Resources (http://www.conservation.ca.gov/dog). The *P* wave onset times were picked using the Suspension Bridge Picking (SBPx) algorithm (https://www.mathworks.com/matlabcentral/fileexchange/51996-suspension-bridge-picking-algorithm--sbpx-). The stress was inverted using the open-access Matlab code STRESSINVERSE (http://www.ig.cas.cz/stress-inverse).

References

Beall, J., & Wright, M. (2010). Southern extent of The Geysers high temperature reservoir based on seismic and geochemical evidence. *Geothermal Resources Council Transactions*, *34*, 1199–1202.

Beall, J., Wright, M., Pingol, A., & Atkinson, P. (2010). Effect of high rate injection on seismicity in The Geysers. *Geothermal Resources Council Transactions*, *34*, 1203–1208.

Boyd, O. S., Dreger, D. S., Lai, V. H., & Gritto, R. (2015). A systematic analysis of seismic moment tensor at The Geysers geothermal field, California. *Bulletin of the Seismological Society of America*, *105*(6), 2969–2986. https://doi.org/10.1785/0120140285

Boyle, K., & Zoback, M. (2014). The stress state of the Northwest Geysers, California geothermal field, and implications for fault-controlled fluid flow. *Bulletin of the Seismological Society of America*, *104*(5), 2303–2312. https://doi.org/10.1785/0120130284

Davi, R., & Vavryčuk, V. (2012). Seismic network calibration for retrieving accurate moment tensors. *Bulletin of the Seismological Society of America*, *102*(6), 2491–2506. https://doi.org/10.1785/0120110344

Dellinger, M., Majer, E. L., Freeman, K., Johnson, L., Jarpe, S., Nihei, K., et al. (2017). Monitoring the effect of injection of fluids from the Lake County pipeline on seismicity at The Geysers, California, geothermal field (report no. FG-36-03GO13048), Department of Energy, US. https://doi.org/10.2172/1410331

Dreger, D. S., Boyd, O. S., & Gritto, R. (2017). Automatic moment tensor analyses, in-situ stress estimation and temporal stress changes at The Geysers EGS Demonstration Project. Proceedings: 42nd Workshop on Geothermal Reservoir Engineering, Stanford University.

Dreger, D. S., Boyd, O. S., Gritto, R., & Taira, T. a. (2018). Seismic analysis of spatio-temporal fracture generation at The Geysers EGS Demonstration Project. Proceedings: 43rd Workshop on Geothermal Reservoir Engineering, Stanford University.

Eberhart-Phillips, D., & Oppenheimer, D. H. (1984). Induced seismicity in The Geysers geothermal area, California. *Journal of Geophysical Research*, *89*(B2), 1191–1207. https://doi.org/10.1029/JB089iB02p01191

Elkibbi, M., Yang, M., & Rial, J. A. (2005). Crack-induced anisotropy models in The Geysers geothermal field. *Geophysical Journal International*, *162*(3), 1036–1048. https://doi.org/10.1111/j.1365-246X.2005.02697.x

Frohlich, C. (2001). Display and quantitative assessment of distributions of earthquake focal mechanisms. *Geophysical Journal International*, *144*(2), 300–308. https://doi.org/10.1046/j.1365-246x.2001.00341.x

Garcia, J., Hartline, C., Walters, M., Wright, M., Rutqvist, J., Dobson, P. F., & Jeanne, P. (2016). The Northwest Geysers EGS Demonstration Project, California: Part 1: Characterization and reservoir response to injection. *Geothermics*, *63*, 97–119. https://doi.org/10.1016/j.geothermics.2015.08.003

Gritto, R., Dreger, D. S., Boyd, O. S., & Taira, T. a. (2016). Fluid imaging, moment tensors and finite source models during the EGS Demonstration Project at The Geysers, CA. Proceedings: 41st Workshop on Geothermal Reservoir Engineering, Stanford University.

Guilhem, A., Hutchings, L., Dreger, D. S., & Johnson, L. R. (2014). Moment tensor inversions of M similar to 3 earthquakes in The Geysers geothermal fields, California. *Journal of Geophysical Research: Solid Earth*, *119*, 2121–2137. https://doi.org/10.1002/2013jb010271

Hartline, C. S., Walters, M. A., Wright, M. C., Forson, C. K., & Sadowski, A. J. (2016). Three-dimensional structural model building, induced seismicity analysis, drilling analysis, and reservoir management at The Geysers Geothermal Field, Northern California. Proceedings: 41st Workshop on Geothermal Reservoir Engineering, Stanford University.

Hudson, J. A., Pearce, R. G., & Rogers, R. M. (1989). Source type plot for inversion of the moment tensor. *Journal of Geophysical Research*, *94*(B1), 765–774. https://doi.org/10.1029/JB094iB01p00765

Jeanne, P., Rutqvist, J., Dobson, P. F., Garcia, J., Walters, M., Hartline, C., & Borgia, A. (2015). Geomechanical simulation of the stress tensor rotation caused by injection of cold water in a deep geothermal reservoir. *Journal of Geophysical Research: Solid Earth*, *120*, 8422–8438. https://doi.org/10.1002/2015JB012414

Jeanne, P., Rutqvist, J., Rinaldi, A. P., Dobson, P. F., Walters, M., Hartline, C., & Garcia, J. (2015). Seismic and aseismic deformations and impact on reservoir permeability: The case of EGS stimulation at The Geysers, California, USA. *Journal of Geophysical Research: Solid Earth*, *120*, 7863–7882. https://doi.org/10.1002/2015jb012142

Johnson, C. W., Totten, E. J., & Burgmann, R. (2016). Depth migration of seasonally induced seismicity at The Geysers geothermal field. *Geophysical Research Letters*, *43*, 6196–6204. https://doi.org/10.1002/2016GL069546

Johnson, L. R. (2014a). A source model for induced earthquakes at The Geysers geothermal reservoir. *Pure and Applied Geophysics*, *171*(8), 1625–1640. https://doi.org/10.1007/s00024-014-0798-7

Johnson, L. R. (2014b). Source mechanisms of induced earthquakes at The Geysers geothermal reservoir. *Pure and Applied Geophysics*, *171*(8), 1641–1668. https://doi.org/10.1007/s00024-014-0795-x

Jousset, P., Gritto, R., Haberland, C., & Hartline, C. (2013). Broadband seismological observations at The Geysers geothermal area, California, USA. Paper presented at the EGU General Assembly Conference Abstracts.

Julian, B., Miller, A., & Foulger, G. (1993). Non-shear focal mechanisms of earthquakes at The Geysers, California and Hengill, Iceland, geothermal areas. *Geothermal Resources Council Transactions*, *17*, 123–128.

Kwiatek, G., Martínez-Garzón, P., Dresen, G., Bohnhoff, M., Sone, H., & Hartline, C. (2015). Effects of long-term fluid injection on induced seismicity parameters and maximum magnitude in northwestern part of The Geysers geothermal field. *Journal of Geophysical Research: Solid Earth*, *120*, 7085–7101. https://doi.org/10.1002/2015jb012362

Lou, M., Shalev, E., & Malin, P. E. (1997). Shear-wave splitting and fracture alignments at the Northwest Geysers, California. *Geophysical Research Letters*, *24*(15), 1895–1898. https://doi.org/10.1029/97GL01845

Majer, E. L., & Peterson, J. E. (2007). The impact of injection on seismicity at The Geysers, California geothermal field. *International Journal of Rock Mechanics and Mining Sciences*, *44*(8), 1079–1090. https://doi.org/10.1016/j.ijrmms.2007.07.023

Martínez-Garzón, P., Bohnhoff, M., Kwiatek, G., & Dresen, G. (2013). Stress tensor changes related to fluid injection at The Geysers geothermal field, California. *Geophysical Research Letters*, *40*, 2596–2601. https://doi.org/10.1002/grl.50438

Martínez-Garzón, P., Kwiatek, G., Bohnhoff, M., & Dresen, G. (2016). Impact of fluid injection on fracture reactivation at The Geysers geothermal field. *Journal of Geophysical Research: Solid Earth*, *121*, 7432–7449. https://doi.org/10.1002/2016JB013137

Martínez-Garzón, P., Kwiatek, G., Bohnhoff, M., & Dresen, G. (2017). Volumetric components in the earthquake source related to fluid injection and stress state. *Geophysical Research Letters*, *44*, 800–809. https://doi.org/10.1002/2016GL071963

Martínez-Garzón, P., Kwiatek, G., Sone, H., Bohnhoff, M., Dresen, G., & Hartline, C. (2014). Spatiotemporal changes, faulting regimes, and source parameters of induced seismicity: A case study from The Geysers geothermal field. *Journal of Geophysical Research: Solid Earth*, *119*, 8378–8396. https://doi.org/10.1002/2014jb011385

Michael, A. J. (1984). Determination of stress from slip data: faults and folds. *Journal of Geophysical Research: Solid Earth*, *89*(B13), 11,517–11,526.

O'Connell, D. R., & Johnson, L. R. (1988). Second-order moment tensors of microearthquakes at The Geysers geothermal field, California. *Bulletin of the Seismological Society of America*, *78*(5), 1674–1692.

Oppenheimer, D. H. (1986). Extensional tectonics at The Geysers geothermal area, California. *Journal of Geophysical Research*, *91*(B11), 11,463–11,476. https://doi.org/10.1029/JB091iB11p11463

Provost, A.-S., & Houston, H. (2003). Stress orientations in Northern and Central California: Evidence for the evolution of frictional strength along the San Andreas plate boundary system. *Journal of Geophysical Research*, *108*(B3), 2175. https://doi.org/10.1029/2001JB001123

Ross, A., Foulger, G. R., & Julian, B. R. (1996). Non-double-couple earthquake mechanisms at The Geysers geothermal area, California. *Geophysical Research Letters*, *23*(8), 877–880. https://doi.org/10.1029/96GL00590

Ross, A., Foulger, G. R., & Julian, B. R. (1999). Source processes of industrially-induced earthquakes at The Geysers geothermal area, California. *Geophysics*, *64*(6), 1877–1889. https://doi.org/10.1190/1.1444694

Rutqvist, J., Jeanne, P., Dobson, P. F., Garcia, J., Hartline, C., Hutchings, L., et al. (2016). The Northwest Geysers EGS Demonstration Project, California - Part 2: Modeling and interpretation. *Geothermics*, *63*, 120–138. https://doi.org/10.1016/j.geothermics.2015.08.002

Sadowski, A. J., Forson, C. K., Walters, M. A., & Hartline, C. S. (2016). Compilation surface geologic map for use in three-dimensional structural model building at The Geysers geothermal field, Northern California. Proceedings: 41st Workshop on Geothermal Reservoir Engineering, Stanford University.

Segall, P., & Fitzgerald, S. D. (1998). A note on induced stress changes in hydrocarbon and geothermal reservoirs. *Tectonophysics*, *289*(1-3), 117–128. https://doi.org/10.1016/S0040-1951(97)00311-9

Stark, M. (2003). Seismic evidence for a long-lived enhanced geothermal system (EGS) in the Northern Geysers reservoir. *Geothermal Resources Council Transactions*, *27*, 727–732.

Stierle, E., Bohnhoff, M., & Vavryčuk, V. (2014). Resolution of non-double-couple components in the seismic moment tensor using regional networks—II: Application to aftershocks of the 1999 M-w 7.4 Izmit earthquake. *Geophysical Journal International*, *196*(3), 1878–1888. https://doi.org/10.1093/gji/ggt503

Stierle, E., Vavryčuk, V., Šílený, J., & Bohnhoff, M. (2014). Resolution of non-double-couple components in the seismic moment tensor using regional networks-I: A synthetic case study. *Geophysical Journal International*, *196*(3), 1869–1877. https://doi.org/10.1093/gji/ggt502

Thomas, R. P., Chapman, R. H., & Dykstra, H. (1986). *A reservoir assessment of The Geysers geothermal field* (Vol. TR27). Sacramento, CA: California Department of Conservation, Division of Oil & Gas.

Vavryčuk, V. (2001). Inversion for parameters of tensile earthquakes. *Journal of Geophysical Research*, *106*(B8), 16,339–16,355. https://doi.org/10.1029/2001JB000372

Vavryčuk, V. (2005). Focal mechanisms in anisotropic media. *Geophysical Journal International*, *161*(2), 334–346.

Vavryčuk, V. (2011a). Principal earthquakes: Theory and observations from the 2008 West Bohemia swarm. *Earth and Planetary Science Letters*, *305*(3–4), 290–296. https://doi.org/10.1016/j.epsl.2011.03.002

Vavryčuk, V. (2011b). Tensile earthquakes: Theory, modeling, and inversion. *Journal of Geophysical Research*, *116*, B12320. https://doi.org/10.1029/2011JB008770

Vavryčuk, V. (2014). Iterative joint inversion for stress and fault orientations from focal mechanisms. *Geophysical Journal International*, *199*(1), 69–77. https://doi.org/10.1093/gji/ggu224

Vavryčuk, V. (2015). Moment tensor decompositions revisited. *Journal of Seismology*, *19*(1), 231–252. https://doi.org/10.1007/s10950-014-9463-y

Vavryčuk, V., Adamová, P., Doubravová, J., & Jakoubková, H. (2017). Moment tensor inversion based on the principal component analysis of waveforms: Method and application to microearthquakes in West Bohemia, Czech Republic. *Seismological Research Letters*, *88*(5), 1303–1315. https://doi.org/10.1785/0220170027

Vavryčuk, V., Bohnhoff, M., Jechumtálová, Z., Kolář, P., & Šílený, J. (2008). Non-double-couple mechanisms of microearthquakes induced during the 2000 injection experiment at the KTB site, Germany: A result of tensile faulting or anisotropy of a rock? *Tectonophysics*, *456*(1–2), 74–93.

Waldhauser, F. (2009). Near-real-time double-difference event location using long-term seismic archives, with application to Northern California. *Bulletin of the Seismological Society of America*, *99*(5), 2736–2748. https://doi.org/10.1785/0120080294

Waldhauser, F., & Schaff, D. P. (2008). Large-scale relocation of two decades of Northern California seismicity using cross-correlation and double-difference methods. *Journal of Geophysical Research*, *113*, B08311. https://doi.org/10.1029/2007JB005479

Zang, A., Oye, V., Jousset, P., Deichmann, N., Gritto, R., McGarr, A., et al. (2014). Analysis of induced seismicity in geothermal reservoirs—An overview. *Geothermics*, *52*, 6–21. https://doi.org/10.1016/j.geothermics.2014.06.005

Zoback, M. D. (2007). *Reservoir geomechanics*. Cambridge: Cambridge University Press. https://doi.org/10.1017/CBO9780511586477